The Journal of Chemical Physics

RESEARCH ARTICLE | JANUARY 22 2025

Mixed atomistic–implicit quantum/classical approach to molecular nanoplasmonics

Pablo Grobas Illobre ; Piero Lafiosca ; Luca Bonatti ; Tommaso Giovannini ; Chiara Cappelli

Check for updates

J. Chem. Phys. 162, 044103 (2025)

https://doi.org/10.1063/5.0245629

AIP Publishing

The Journal of Chemical Physics ARTICLE pubs.aip.org/aip/jcp

Mixed atomistic–implicit quantum/classical approach to molecular nanoplasmonics

Cite as: J. Chem. Phys. **162**, 044103 (2025); doi: 10.1063/5.0245629
Submitted: 28 October 2024 • Accepted: 3 January 2025 •
Published Online: 22 January 2025

Pablo Grobas Illobre,[1] **Piero Lafiosca,**[1] **Luca Bonatti,**[1] **Tommaso Giovannini,**[2,a)] **and Chiara Cappelli**[1,3,a)]

AFFILIATIONS

[1] Scuola Normale Superiore, Piazza dei Cavalieri 7, 56126 Pisa, Italy
[2] Department of Physics, University of Rome Tor Vergata, Via della Ricerca Scientifica 1, 00133 Rome, Italy
[3] IMT School for Advanced Studies Lucca, Piazza San Francesco 19, Lucca 55100, Italy

[a)] **Authors to whom correspondence should be addressed:** tommaso.giovannini@uniroma2.it and chiara.cappelli@sns.it

ABSTRACT

A multiscale quantum mechanical (QM)/classical approach is presented that is able to model the optical properties of complex nanostructures composed of a molecular system adsorbed on metal nanoparticles. The latter is described by a combined atomistic–continuum model, where the core is described using the implicit boundary element method (BEM) and the surface retains a fully atomistic picture and is treated employing the frequency-dependent fluctuating charge and fluctuating dipole (ωFQFμ) approach. The integrated QM/ωFQFμ-BEM model is numerically compared with state-of-the-art fully atomistic approaches, and the quality of the continuum/core partition is evaluated. The method is then extended to compute surface-enhanced Raman scattering within a time-dependent density functional theory framework.

I. INTRODUCTION

When metal nanoparticles (NPs) are irradiated with external radiation, coherent oscillations of conduction electrons, also named localized surface plasmons (LSPs), can be excited.[1–3] Most NP optical properties are related to LSP peculiar properties, which can be tuned by varying the NP's size, shape, and chemical composition.[4] Plasmonic nanostructures can enhance, control, or suppress properties of molecules interacting with light: these features are exploited in molecular nanoplasmonics.[5–10] A deep understanding of the phenomena that occur at the molecular and nanoscale in the presence of light can be achieved by exploiting multiscale hybrid techniques, which use different levels of description for molecules and plasmonic nanosystems.[5,11] With these methods, a reliable representation of both atomistic details and collective features, such as plasmons, in these complex systems can be achieved.

In principle, the ideal theoretical approach to molecular nanoplasmonics should rely on a quantum mechanical (QM) description of the whole system (molecule + nanostructured substrate). However, due to their unfavorable computational scaling, full *ab initio* methods are currently limited to small model systems (generally, <100 atoms), in contrast to the large size of plasmonic substrates, which typically comprise thousands or millions of atoms.[12–16] To address these limitations, hybrid multiscale QM/classical approaches have been developed,[11,17,18] where the molecular adsorbate is treated at the QM level, while the substrate's plasmonic response is calculated by using classical electrodynamical methods, substantially reducing the computational cost. The most crude classical description of the plasmonic response of a metal NP is given by continuum implicit approaches, such as the Mie theory,[19] the Finite Difference Time Domain (FDTD),[20] or the Boundary Element Method (BEM),[21–24] which completely disregard the NP atomistic nature. To overcome this limitation, fully atomistic approaches have been developed, such as Discrete Interaction Models (DIMs)[17,18,25–30] and the Frequency-Dependent Fluctuating Charges and Fluctuating Dipoles (ωFQFμ) approach.[11,24,31–39] ωFQFμ can correctly reproduce QM results for metal NPs even below the quantum limit (<5 nm),[35] capture the plasmonic properties of systems featuring subnanometer junctions,[31] defects,[34,36] treat bimetallic particles,[37] and colloidal nanostructures.[39] In addition, it describes noble metal NPs[35] and graphene-based structures under the same theoretical framework.[32] Both families (implicit and atomistic) have pros and cons. Continuum models feature a favorable computational cost, which scales with the size of the NP surface, facilitating the description of large systems.[23,40–46] However, their implicit, non-atomistic nature fails at capturing the NP plasmonic response in specific configurations characterized by atomistic defects, sub-nanometer junctions, and sharp interfaces,[45,47] which are associated with huge enhancements of the electric field (the so-called hot-spots). Conversely, while atomistic approaches appropriately capture these features, they become computationally less efficient as the size of the system increases, because their computational cost scales with the number of atoms, i.e., the NP volume.[33]

This work proposes a novel multiscale approach specifically designed to overcome the limitations associated with atomistic and continuum approaches. The method, which is here specified for noble metal NPs, describes the core with an implicit approach, by using the BEM method, while the NP surface is treated at the fully atomistic approach, by means of ωFQFμ. The resulting ωFQFμ-BEM approach constitutes, to the best of our knowledge, the first hybrid atomistic–continuum methodology to evaluate the optical response of plasmonic substrates within classical electrodynamics. Furthermore, ωFQFμ-BEM is coupled to a QM description of a molecular adsorbate described at the Time-Dependent Density Functional Theory (TDDFT) level, allowing for the calculation of molecular properties and signals in the vicinity of plasmonic nanostructures.[11,42,48]

One of the most interesting aspects of molecular nanoplasmonics is the huge enhancement of the induced electric field in the NP surface proximity, which can drastically affect the electronic properties of molecular adsorbates. As a result, molecular spectral signals can be significantly enhanced, providing an invaluable platform for molecular sensing. The most diffuse technique that exploits this effect is Surface Enhanced Raman Scattering (SERS),[2,6,10,14,49–57] where the molecular Raman signals are enhanced by several orders of magnitude, allowing single molecule detection. SERS is at present used in various applicative fields, such as catalysis, chemical biology, biophysics, and biomedicine.[58–65] For this reason, in this paper, QM/ωFQFμ-BEM is extended to compute SERS signals.

This paper is organized as follows: In Sec. II, ωFQFμ and BEM methods are briefly recalled, and the novel ωFQFμ-BEM and QM/ωFQFμ-BEM models are presented. After a brief section reporting on the computational details, the methods are validated by computing NPs optical properties and SERS spectra of pyridine with the novel approaches or employing reference fully atomistic methods (ωFQFμ and QM/ωFQFμ). Conclusions and future perspectives end the paper.

II. THEORY

This section gives an overview of the theoretical background leading to the formulation of the QM/ωFQFμ-BEM approach. First, the integration of the ωFQFμ and BEM models is discussed, and the ωFQFμ-BEM equations are presented to replicate the plasmonic response of fully atomistic NPs as built by a continuum BEM core within an atomistic ωFQFμ shell (see Fig. 1). Then, the QM/ωFQFμ-BEM coupling is developed and specified to describe the SERS of a molecule, studied at the TDDFT level, placed in the vicinity of the plasmonic NP.

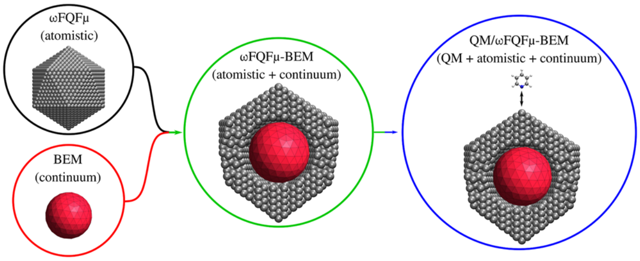

FIG. 1. Graphical representation of ωF-QFμ, BEM, ωFQFμ-BEM, and QM/ωFQFμ-BEM approaches.

A. Classical models for plasmonics

1. Frequency-dependent fluctuating charges and fluctuating dipoles (ωFQFμ) for plasmonic metal nanoparticles

ωFQFμ is a classical, fully atomistic model that accurately reproduces the plasmonic behavior of noble metal nanostructures.[31,35] In ωFQFμ, each atom is endowed with a complex electric charge (q) describing intraband transitions[24,31–34] and a complex dipole ($\boldsymbol{\mu}$) capturing the interband contributions to the optical response.[11,35,37] Both charges and dipoles are formulated within the quasistatic regime; therefore, retardation effects are neglected.[31,35,37] Combining the description of the time-dependent charge fluctuation on atom i with the Drude model for evaluating the momentum derivative, the following equation, in the frequency domain, holds:[31]

$$-\,\mathrm{i}\omega q_i(\omega) = \sum_j 2n_0 \mathscr{A}_{ij} \frac{\langle \mathbf{E}(\omega)\rangle}{1/\tau - \mathrm{i}\omega} \cdot \vec{l}_{ji}, \tag{1}$$

where $q_i(\omega)$ is the charge lying on atom i and oscillating at frequency ω, n_0 is the atomic density, and τ is the scattering time. $\mathscr{A}_{ij}$ is the effective area ruling charge exchange between atoms i and j, $\vec{l}_{ji}$ is the unit vector that connects both atoms, and $\langle \mathbf{E}(\omega)\rangle$ is the electric field averaged over all trajectories.

Equation (1) can be linked to atomic properties through the electrochemical potential (ϕ^{el}) by approximating $\langle \mathbf{E}(\omega)\rangle \cdot \vec{l}_{ji} \approx (\phi^{el}_j - \phi^{el}_i)/l_{ij}$, yielding the following expression:[31]

$$-\,i\omega q_i(\omega) = \frac{2n_0\tau}{1 - i\omega\tau} \sum_j^N \left[1 - f(r_{ij})\right] \frac{\mathscr{A}_{ij}}{r_{ij}} (\phi^{el}_j - \phi^{el}_i), \tag{2}$$

where $f(r_{ij})$ serves as a phenomenological Fermi damping function designed to limit charge transfer to neighboring atoms. This function also mimics the characteristic profile of quantum tunneling, which is dependent on the distance between atoms (r_{ij}), and it has been parameterized against *ab initio* data.[31,35,37] ϕ^{el}_i is the electrochemical potential acting on the i-th atom, which includes the potential generated by the external electric field, the charges, and the dipoles.

ωFQFμ dipoles add a further source of polarization, which is crucial for modeling the physics of d-electrons.[66–68] This is achieved by incorporating a complex frequency-dependent atomic polarizability α_i^ω, extracted from the experimental permittivity, which encloses the effect of interband transitions. The atomic dipoles can then be computed as follows:[35]

$$\boldsymbol{\mu}_i(\omega) = \alpha_i^\omega \mathbf{E}_i^{\text{tot}}, \tag{3}$$

where $\boldsymbol{\mu}_i(\omega)$ is the complex frequency-dependent atomic dipole on atom i. $\mathbf{E}_i^{\text{tot}}$ represents the total electric field acting on the i-th atomic position and is the superposition of the external electric field and the electric field generated by the dipoles and charges.

Equations (2) and (3) can be reformulated into the following set of linear equations:[35]

$$\begin{aligned}\sum_{j=1}^{N}\left(\sum_{k=1}^{N}\overline{K}_{ik}(\mathbf{T}_{kj}^{\text{qq}}-\mathbf{T}_{ij}^{\text{qq}})+\mathrm{i}\frac{\omega}{w(\omega)}\delta_{ij}\right)q_j&\\ +\sum_{j=1}^{N}\left(\sum_{k=1}^{N}\overline{K}_{ik}(\mathbf{T}_{kj}^{\text{q}\mu}-\mathbf{T}_{ij}^{\text{q}\mu})\right)\boldsymbol{\mu}_j&=\sum_{k=1}^{N}\overline{K}_{ik}(\mathbf{V}_i^{\text{ext}}-\mathbf{V}_k^{\text{ext}}),\end{aligned} \tag{4}$$

$$\sum_{j\neq i}^{N}\mathbf{T}_{ij}^{\mu\text{q}}q_j+\sum_{j\neq i}^{N}\mathbf{T}_{ij}^{\mu\mu}\boldsymbol{\mu}_j+\frac{1}{\alpha_i^\omega}\boldsymbol{\mu}_i=\mathbf{E}_i^{\text{ext}}, \tag{5}$$

where $\mathbf{T}^{\text{qq}}$, $\mathbf{T}^{\text{q}\mu}$, and $\mathbf{T}^{\mu\mu}$ are the charge–charge, charge–dipole, and dipole–dipole interaction kernels, respectively;[31,35,69] and $\mathbf{V}_i^{\text{ext}}$ and $\mathbf{E}_i^{\text{ext}}$ are the potential and the electric field generated by the external radiation at each of the i-th atomic positions, respectively. In ωFQFμ, the charges and dipoles are associated with a Gaussian-type density distribution; thus, the interaction kernels are obtained as first proposed by Mayer.[70] Finally, $w(\omega)$ and $\overline{K}_{ij}$ are defined as follows:[33,35]

$$w(\omega) = \frac{2n_0}{1/\tau - \mathrm{i}\omega}, \tag{6}$$

$$\overline{K}_{ij} = (1 - f(r_{ij}))\frac{\mathcal{A}_{ij}}{r_{ij}}. \tag{7}$$

By defining $\mathbf{T}_{ii}^{\mu\mu} = 1/\alpha^\omega$, Eqs. (4) and (5) can be recast as follows:[35]

$$\left[\begin{pmatrix}\mathbf{A}^{q} & \mathbf{A}^{q\mu}\\ \mathbf{T}^{\mu\text{q}} & \mathbf{T}^{\mu\mu}\end{pmatrix}-\begin{pmatrix}z(\omega)\mathbf{I}_N & 0\\ 0 & z'(\omega)\mathbf{I}_{3N}\end{pmatrix}\right]\begin{pmatrix}\mathbf{q}\\ \boldsymbol{\mu}\end{pmatrix}=\begin{pmatrix}\mathbf{R}\\ -\mathbf{E}^{\text{ext}}\end{pmatrix}, \tag{8}$$

where $\mathbf{A}^q$ represents the charge–charge terms and $\mathbf{A}^{q\mu}$ collects the charge–dipole interactions. The frequency dependence is gathered in the z and z' terms, and $\mathbf{I}_N$ is the NxN identity matrix. Finally, the external potential and external field effects are included in the right-hand-side matrices $\mathbf{R}$ and $\mathbf{E}^{\text{ext}}$. The reader is referred to Sec. S1 of the supplementary material for the description of each term in Eq. (8).

2. Boundary element method (BEM)

The Boundary Element Method (BEM) constitutes a reliable approach for solving the Polarizable Continuum Model equations applied to the study of plasmonic nanoparticles (PCM-NPs).[41] There, the NP is treated as a homogeneous continuum dielectric by exploiting a classical electrodynamics formalism. Plasmonics is then governed by the frequency-dependent permittivity function chosen to describe the material and that of the media in which it is embedded.[23,24,45,47,71] BEM involves the calculation of surface charges, which yield a global surface charge density that encapsulates the optical response of the system. BEM charges are calculated upon applying the model on a triangular-discretized mesh delimiting the NP surface. At each triangular centroid, a complex point charge that describes the optical response of the material is calculated. This enables the exploration of the plasmonic properties of the analyzed structures, which is influenced by the geometric features of the discretized mesh and by the material's permittivity function.

Here, we rely on the quasistatic PCM-NP framework formulated in the integral equation formalism and numerically solved using BEM. The computation of the BEM charges ($\boldsymbol{\sigma}$) is described as follows:[16,40,45,72,73]

$$\left(2\pi\frac{\varepsilon_2(\omega)+\varepsilon_1(\omega)}{\varepsilon_2(\omega)-\varepsilon_1(\omega)}\mathbf{I}_P+\mathbf{F}\right)\mathbf{S}\mathbf{A}^{-1}\boldsymbol{\sigma}=-(2\pi\mathbf{I}_P+\mathbf{F})\mathbf{V}, \tag{9}$$

where $\varepsilon_1(\omega)$ is the complex dielectric function of the environment [for vacuum $\varepsilon_1(\omega) = 1$] and $\varepsilon_2(\omega)$ that of the NP. $\mathbf{A}$ is a diagonal matrix collecting the area of each triangle or *tessera*. $\mathbf{I}_P$ is the PxP identity matrix, where P is the number of *tesserae*. The matrices $\mathbf{S}$ and $\mathbf{F}$ are defined based on the geometrical characteristics of the mesh. $\mathbf{V}$ collects the values of the electrostatic potential generated by the external electric field at each triangular centroid. For details on the derivation of Eq. (9), the reader is encouraged to refer to Ref. 72.

We can isolate the frequency-dependent terms of Eq. (9) and reformulate them as follows:

$$(\mathbf{B}^{\sigma} - \xi(\omega))\boldsymbol{\sigma} = \mathbf{R}_{\mathbf{B}}. \tag{10}$$

In Sec. S1 of the supplementary material, further details on the $\mathbf{F}$ and $\mathbf{S}$ matrices are given, along with the description of each term in Eq. (10).

3. ωFQFμ-BEM for plasmonic metal nanoparticles

The idea of integrating ωFQFμ and BEM, giving rise to a model that is named ωFQFμ-BEM, arises from their close similarities. In particular, both formalisms are grounded in classical electrodynamics and rely on complex frequency-dependent quantities (charges/dipoles) to describe the optical response of metal NPs. However, these models present notable differences. First, the BEM response is rooted in the permittivity chosen to describe the material and lacks any atomistic description. Conversely, ωFQFμ is based on textbook concepts, such as the Drude model of conduction for describing intraband transitions in terms of fluctuating charges. Interband transitions are recovered through a set of fluctuating dipoles that are defined in terms of the experimental interband polarizability. By this, ωFQFμ can effectively decouple the physical processes influencing the optical response of the plasmonic substrate while also retaining its atomistic nature. However, ωFQFμ encounters scalability challenges, eventually leading to the exploration of alternative strategies to solve Eq. (8).[33,74] Remarkably, ωFQFμ-BEM can alleviate these limitations by representing NPs as built of an internal continuum BEM core and an external atomistic ωFQFμ shell, with substantial computational savings.

The ωFQFμ-BEM coupling is formulated by including the potential and electric field generated by the BEM charges in the ωFQFμ equations, specifically in ϕ^{el} [Eq. (2)] and $\mathbf{E}^{\text{tot}}$ [Eq. (3)], respectively. In addition, the potential generated by the ωFQFμ charges and dipoles needs to be included in the BEM $\mathbf{V}$ matrix [Eq. (9)]. As a result of these modifications, Eqs. (4), (5), and (9) are modified as follows:

$$\begin{aligned}\sum_{j=1}^{N}\left(\sum_{k=1}^{N}\overline{K}_{ik}(\mathbf{T}^{\text{qq}}_{kj}-\mathbf{T}^{\text{qq}}_{ij})+\mathrm{i}\frac{\omega}{w(\omega)}\delta_{ij}\right)q_j\\ +\sum_{j=1}^{N}\left(\sum_{k=1}^{N}\overline{K}_{ik}(\mathbf{T}^{\text{q}\mu}_{kj}-\mathbf{T}^{\text{q}\mu}_{ij})\right)\boldsymbol{\mu}_j\\ +\sum_{\nu=1}^{P}\left(\sum_{k=1}^{N}\overline{K}_{ik}(\mathbf{T}^{\text{q}\sigma}_{k\nu}-\mathbf{T}^{\text{q}\sigma}_{i\nu})\right)\boldsymbol{\sigma}_\nu=\sum_{k=1}^{N}\overline{K}_{ik}(\mathbf{V}^{\text{ext}}_i-\mathbf{V}^{\text{ext}}_k),\end{aligned}\tag{11}$$

$$\sum_{j\neq i}^{N}\mathbf{T}^{\mu\text{q}}_{ij}q_j+\sum_{\nu=1}^{P}\mathbf{T}^{\mu\sigma}_{i\nu}\boldsymbol{\sigma}_\nu+\sum_{j\neq i}^{N}\mathbf{T}^{\mu\mu}_{ij}\boldsymbol{\mu}_j+\frac{1}{\alpha_i^{\omega}}\boldsymbol{\mu}_i=\mathbf{E}^{\text{ext}}_i,\tag{12}$$

$$\begin{aligned}\left(2\pi\frac{\varepsilon_2(\omega)+\varepsilon_1(\omega)}{\varepsilon_2(\omega)-\varepsilon_1(\omega)}\mathbf{I}_P+\mathbf{F}\right)(\mathbf{S}\mathbf{A}^{-1})\boldsymbol{\sigma}\\ =-(2\pi\mathbf{I}_P+\mathbf{F})\left(\mathbf{V}^{\text{ext}}+\mathbf{V}^{\boldsymbol{\omega}\mathbf{FQ}}+\mathbf{V}^{\boldsymbol{\omega}\mathbf{F}\boldsymbol{\mu}}\right),\end{aligned}\tag{13}$$

where Eqs. (11) and (12) include the effect of the BEM charges ($\boldsymbol{\sigma}$) in the calculation of the ωFQFμ charges ($\mathbf{q}$) and dipoles ($\boldsymbol{\mu}$), respectively. Equation (13) extends BEM, including the potential generated by the ωFQFμ charges $\mathbf{V}^{\boldsymbol{\omega}\mathbf{FQ}}=\mathbf{T}^{\sigma\text{q}}_{\nu i}q_i$ and dipoles $\mathbf{V}^{\mathbf{F}\boldsymbol{\mu}}=\mathbf{T}^{\sigma\mu}_{\nu i}\mu_i$. $\mathbf{T}^{\sigma\text{q}}$ and $\mathbf{T}^{\sigma\mu}$ are the interaction kernels of BEM point charges with ωFQFμ charges and dipoles described by Gaussian functions, respectively (see Sec. S1 of the supplementary material for more details).[31,35,75]

Finally, the linear problem represented by equations Eqs. (11)–(13) can be expressed in compact matrix notation as follows:

$$\left[\left(\begin{array}{cc|c}\mathbf{A}^{q} & \mathbf{A}^{q\mu} & \mathbf{A}^{q\sigma}\\ \mathbf{T}^{\mu q} & \mathbf{T}^{\mu\mu} & \mathbf{T}^{\mu\sigma}\\ \hline \mathbf{B}^{\sigma q} & \mathbf{B}^{\sigma\mu} & \mathbf{B}^{\sigma}\end{array}\right)-\left(\begin{array}{cc|c}z(\omega)\mathbf{I}_N & 0 & 0\\ 0 & z'(\omega)\mathbf{I}_N & 0\\ \hline 0 & 0 & \xi(\omega)\end{array}\right)\right]\left(\begin{array}{c}\mathbf{q}\\ \mu\\ \hline \sigma\end{array}\right)=\left(\begin{array}{c}\mathbf{R}\\ -\mathbf{E}^{\text{ext}}\\ \hline \mathbf{R}_{\mathbf{B}}\end{array}\right).\tag{14}$$

The terms in Eq. (14) are detailed in Sec. S1 of the supplementary material.

B. QM/ωFQFμ-BEM model and its extension to SERS

Once ωFQFμ-BEM has been formulated, it can be coupled to a QM description of a molecular system in a QM/Classical fashion,[5,17,23,76–80] giving rise to the QM/ωFQFμ-BEM model. ωFQFμ-BEM describes the system's response to external oscillating electric fields; therefore, it can be naturally translated into a linear response formalism. The coupling is done by following the same strategy that was exploited to formulate the two-layer QM/ωFQFμ approach.[11]

In this scenario, considering the Kohn–Sham operators generated in a grid of points exploiting a numerical integration strategy,[81] the ωFQFμ-BEM perturbation operator (V^{pert}) modifying the electronic density has the following expression:

$$\begin{aligned}V^{\text{pert}}(\mathbf{r},\omega)&=V^{\text{ext}}(\mathbf{r},\omega)+V^{\text{loc}}(\mathbf{r},\omega),\\ V^{\text{loc}}(\mathbf{r},\omega)&=\sum_{l=1}^{N}q_l^{\text{ext}}(\omega)\mathbf{T}^{(0)}(d_l)+\sum_{l=1}^{N}\boldsymbol{\mu}_l^{\text{ext}}(\omega)\cdot\mathbf{T}^{(1)}(d_l)\\ &\quad+\sum_{l=1}^{P}\sigma_l^{\text{ext}}(\omega)\mathbf{T}^{(0)}(d_l),\end{aligned}$$

where $q^{\text{ext}}(\omega)$, $\mu^{\text{ext}}(\omega)$, and $\sigma^{\text{ext}}(\omega)$ are calculated using Eq. (14), where V^{ext} is the potential originating them. Furthermore, d_l is the distance between the l-th atom or *tessera* centroid and a generic grid point, while $\mathbf{T}^{(0)}$ and $\mathbf{T}^{(1)}$ are the charge-to-grid and dipole-to-grid interaction kernels, respectively.[11,82]

Considering the notation that the $(i,j)/(a,b)$ indices run over occupied/virtual Kohn–Sham molecular orbitals, the first-order density with respect to the external field component α [$\rho^{\alpha}(\mathbf{r},\omega)$] is expressed as follows:

$$\rho^{\alpha}(\mathbf{r},\omega)=\sum_{ia}P^{\alpha}_{ia}(\omega)\Psi_i(\mathbf{r})\Psi_a^*(\mathbf{r})+P^{\alpha}_{ai}\Psi_a(\mathbf{r})\Psi_i^*(\mathbf{r}),\tag{15}$$

where $\Psi(\mathbf{r})$ represents Khon–Sham orbitals and $P^{\alpha}(\omega)$ is the first-order density matrix considering the α component of the external field.

The matrix elements of $\mathbf{P}^{\alpha}(\omega)$ can be obtained from the solution of the linear response equations within the Time-Dependent Kohn–Sham (TDKS) framework,[42,48,83]

$$\left[\begin{pmatrix}\mathbf{A} & \mathbf{B}\\ \mathbf{B}^* & \mathbf{A}^*\end{pmatrix}-(\omega+\mathrm{i}\Gamma)\begin{pmatrix}\mathbf{I} & 0\\ 0 & -\mathbf{I}\end{pmatrix}\right]\begin{pmatrix}\mathbf{X}\\ \mathbf{Y}\end{pmatrix}=-\begin{pmatrix}\mathbf{Q}\\ \mathbf{Q}*\end{pmatrix}.\tag{16}$$

In the QM/ωFQFμ-BEM approach, the terms entering the linear system in Eq. (16) are modified to account for the presence of the ωFQFμ and BEM layers, i.e.,

$$\begin{aligned}A_{ai,bj}&=(\varepsilon_a-\varepsilon_i)\delta_{ab}\delta_{ij}+(ai|bj)-c_x(ab|ij)\\ &\quad+c_l f^{xc}_{ai,bj}+C^{\text{QM}/\omega\text{FQF}\mu-\text{BEM}}_{ai,bj},\\ B_{ai,bj}&=(ai|bj)-c_x(aj|ib)+C^{\text{QM}/\omega\text{FQF}\mu-\text{BEM}}_{ai,bj},\\ Q_{ia}&=\langle\phi_i|V^{\alpha,\text{pert}}(\text{r},\omega)|\phi_a\rangle.\end{aligned}\tag{17}$$

In Eq. (16), $\mathbf{X}$ and $\mathbf{Y}$ are the excitation and de-excitation transition densities, respectively, while Γ is a phenomenological damping factor. ε is the molecular orbital energy, $(ai|bj)$ denotes two-electron integrals, and the c_x, c_l parameters vary depending on the DFT functional employed. In addition, $\mathbf{C}^{\text{QM}/\omega\text{FQF}\mu\text{-BEM}}$ describes the polarization induced by the ωFQFμ-BEM charges and dipoles, which respond to the perturbed TDKS density.[11,17,84] On the right-hand-side, $Q_{ia}=\langle\phi_i|V^{\alpha\text{pert}}(\text{r},\omega)|\phi_a\rangle$ represents the expectation value of the perturbation operator polarized along α.

QM/ωFQFμ-BEM can be extended to compute SERS spectra of molecular systems in the vicinity of metal NPs. To this end, the complex polarizability tensor $\bar{\alpha}_{\alpha\beta}$ needs to be computed,[11,85] where α/β represent the Cartesian components (x,y,z). After solving Eq. (16), $\bar{\alpha}_{\alpha\beta}$ can be calculated as follows:

$$\bar{\alpha}_{\alpha\beta}(\omega;\omega')=-\text{tr}\left[\mathbf{Q}^{\alpha}(\omega)\mathbf{P}^{\beta}(\omega')\right],\tag{18}$$

where $\mathbf{Q}^{\alpha}(\omega)$ is calculated as shown in Eq. (17) and includes the QM dipole and the ωFQFμ-BEM local field operators polarized along α.[11,18,40,86]

According to Placzek's theory of Raman scattering,[87] the Raman signal can be modeled from the frequency-dependent polarizability tensor. Assuming the frequency of the incident and scattered fields to coincide, the Raman intensity related to the k-th normal mode I^k of the QM molecule is given by[11,44,87–89]

$$I^k \propto \frac{(\omega-\omega_k)^4}{\omega_k} 45\left[\alpha'_k(\omega-\omega_k;\omega)\right]^2 + 7\left[\gamma'_k(\omega-\omega_k;\omega)\right]^2, \qquad (19)$$

where ω is the incident frequency, while ω_k and α'_k/γ'_k are the frequency and the isotropic/anisotropic polarizability derivatives associated with the k-th normal mode (Q_k), respectively. They are expressed as follows:[11]

$$\left[\alpha'_k(\omega;\omega')\right]^2 = \frac{1}{9}\left|\sum_{i=x,y,z}\frac{\partial\tilde{\alpha}_{ii}(\omega;\omega')}{\partial Q_k}\right|^2,$$

$$\left[\gamma'_k(\omega;\omega')\right]^2 = \frac{1}{2}\left(\frac{3}{4}\sum_{ij=x,y,z}\left|\frac{\partial\tilde{\alpha}_{ij}(\omega;\omega')}{\partial Q_k}+\frac{\partial\tilde{\alpha}_{ji}(\omega;\omega')}{\partial Q_k}\right|^2 - 9\left[\alpha'_k(\omega;\omega')\right]^2\right).$$

III. COMPUTATIONAL DETAILS

Ag structures are created by using the Atomic Simulation Environment (ASE) Python module v. 3.17.[90] In particular, Ag atoms are disposed in a Face-Centered Cubic (FCC) arrangement defined by a lattice parameter of 4.08 Å. Two morphologies are studied: spherical and icosahedral (Ih) NPs. For ωFQFμ calculations, the parameters defined in Ref. 35 are exploited. Detailed information regarding the geometrical characteristics of all atomistic structures is reported in Tables S2–S5 of the supplementary material.

The continuum BEM meshes representing the surfaces of both spherical and Ih NPs are constructed by using the GMSH software.[91] The frequency-dependent permittivities proposed by Palik,[92] Brendel-Bormann,[93] and Johnson and Christy[94] are exploited in BEM calculations.

ωFQFμ-BEM spherical and Ih structures are built as a core, described as an implicit spherical NP and treated at the BEM level, surrounded by an atomistic shell, treated at the ωFQFμ level. To validate the novel approach, we investigate the variation of the optical response of a spherical Ag nanostructure (radius 4 nm) as a function of the method parameters, namely, the core-to-shell distance, the thickness of the atomistic shell, the BEM *tessellation*, and the dielectric function to describe BEM response.

In particular, we study the optical response as a function of the minimum core-to-shell distance, which varies from 2.88 to 5.76 Å, corresponding to integer multiples of the nearest neighbor distance (2.88 Å) in the studied FCC lattices. For Ag Ih structures, the atomistic shell is defined, ensuring a minimum thickness of three atomic layers in the thinner region.

In ωFQFμ-BEM, the total complex dipole of the NP $(\bar{\zeta})$ is computed as follows:

$$\bar{\zeta}(\omega) = \sum_{i}^{N} q_i(\omega)\mathbf{r}_i + \sum_{i}^{N}\boldsymbol{\mu}_i(\omega) + \sum_{\nu}^{P}\sigma_\nu(\omega)\mathbf{s}_\nu,$$

where $\mathbf{r}_i$ and $\mathbf{s}_\nu$ are the positions of the i-th atom and of the ν-th *tessera* centroid, respectively. From $\bar{\zeta}$, the NP complex frequency-dependent polarizability $(\bar{\xi})$ and the absorption cross section (σ^{abs}) can be calculated as follows:

$$\bar{\xi}(\omega)_{\alpha\beta} = \frac{\bar{\zeta}_\alpha}{E_{0,\beta}} \Longrightarrow \sigma^{\mathrm{abs}}(\omega) = \frac{4\pi\omega}{3c}\,\mathrm{Tr}\,(\bar{\xi}), \qquad (20)$$

where $\alpha\beta$ indicates the polarization of the incident electric field (E_0), and c is the speed of light.

After validating ωFQFμ-BEM, we exploit the multiscale QM/ωFQFμ-BEM to calculate SERS signals of pyridine adsorbed on Ag Ih NPs (with radius varying from 1.9 to 3.8 nm). SERS spectra are computed by representing the Ag Ih NP at the fully atomistic ωFQFμ, implicit BEM, and hybrid ωFQFμ-BEM levels, thus allowing for validating the novel method by a robust comparison with state-of-the-art methods. In all cases, pyridine is placed longitudinally at a distance of 3 Å from the NP surface. Such distance is calculated from the nitrogen atom to the nearest NP atom/*tessera* centroid defining the tip of the atomistic/continuum surface of Ag Ih structures.

In all calculations, pyridine is described at the QM level utilizing the BP86 functional and a double-ζ-polarized DZP basis set, in agreement with previous studies.[11,86] TDDFT equations are solved by imposing a damping factor $\Gamma = 0.01$ eV.[11,86,95,96] α'_k and γ'_k [see Eq. (19)] are calculated by a numerical differentiation scheme, with a constant step size of 0.001 Å.[11,97–99] Normal modes' displacements of pyridine are evaluated *in vacuo*, without explicitly considering NP effects, which are expected to be small for the considered system.[11,86] The influence of the plasmon resonance on SERS signals is assessed by matching the incident light frequency for Raman with the Plasmon Resonance Frequency (PRF) of the NP, whose values are collected in Tables S5 and S6 in the supplementary material. Finally, SERS spectra are plotted using Lorentzian bandshapes characterized by a full width at half maximum (FWHM) of 4 cm^{-1}. QM/ωFQFμ-BEM, QM/ωFQFμ, and QM/BEM calculations are performed by using a locally modified version of the Amsterdam Modeling Suite (AMS).[81]

The NP effect on Raman signals is evaluated through the definition of three observables: the Enhancement Factor (EF), the Maximum Enhancement Factor (MEF), and the Averaged Enhancement Factor (AEF), which are defined as follows:

$$\mathrm{EF}^k(\omega) = \frac{I^k_{\mathrm{NP}}(\omega)}{I^k_{\mathrm{vac}}(\omega)}, \qquad (21)$$

$$\mathrm{MEF}(\omega) = \max_k \mathrm{EF}^k(\omega), \qquad (22)$$

$$\mathrm{AEF}(\omega) = \frac{\sum_k I^k_{\mathrm{NP}}(\omega)}{\sum_l I^l_{\mathrm{vac}}(\omega)}, \qquad (23)$$

where I^k_{NP} and I^k_{vac} are the molecular Raman intensities associated with the k-th normal mode [see Eq. (19)] in the presence of NP and *in vacuo*, respectively. In Eq. (23), k and l indices run over the set of studied molecular normal modes.

A summary of the parameters involved in ωFQFμ, BEM, ωFQFμ-BEM, and SERS calculations is given in Sec. S2.1 of the supplementary material.

IV. RESULTS AND DISCUSSION

In this section, the ωFQFμ-BEM and QM/ωFQFμ-BEM methods are validated by comparison with the reference ωFQFμ and QM/ωFQFμ approaches. In particular, ωFQFμ-BEM is first challenged to reproduce the plasmonic features of spherical NPs by analyzing how a variation of the model parameters affects the optical response. Then, QM/ωFQFμ-BEM is applied to compute SERS of pyridine adsorbed on complex-shaped Ih nanostructures.

A. The ωFQFμ-BEM method for plasmonics

1. Plasmonic features of single nanoparticles

In Fig. 2(a), we show a graphical representation of a spherical NP described at the ωFQFμ-BEM level, constructed by integrating a continuum BEM spherical core within an atomistic ωFQFμ spherical shell. ωFQFμ-BEM spherical NP geometries are defined by four parameters: the radius of the inner BEM core (r_{BEM}), the radii of the outer ωFQFμ shell (R), the BEM core-ωFQFμ shell distance (d), and the difference between the radii of the inner and outer shells (Δr). The computed optical response depends on the proper definition of such parameters, the dielectric function exploited to model the BEM portion, and the number of *tesserae* exploited to mesh the BEM region. It is worth noting that our approach is general, and the full BEM ($r_{\mathrm{BEM}} = R$) or the full ωFQFμ ($\Delta r = R$) description can be easily recovered.

Let us first focus on the computed response for a specific geometry, i.e., a spherical NP with $R = 40.00$ Å, $r_{\mathrm{BEM}} = 20.26$ Å, $\Delta r = 13.98$ Å, and $d = 5.76$ Å. 11 470 atoms constitute the atomistic shell, while the BEM core is defined by 2972 *tesserae*. The Brendel–Bormann frequency-dependent permittivity[93] is exploited to describe the BEM part.

Figure 2(b) compares normalized absorption spectra calculated for ωFQFμ-BEM and the reference, fully atomistic ωFQFμ (hereafter referred to as full-ωFQFμ). The normalization is performed with respect to the full-ωFQFμ PRF absorption. The full-ωFQFμ approach predicts a single absorption peak at 3.47 eV, whereas the ωFQFμ-BEM spectrum features two peaks centered at 2.50 and 3.45 eV. To analyze the physical origin of such a discrepancy, in Fig. 2(c), normalized absorption spectra of the selected spherical NP calculated at the ωFQFμ-BEM level are reported, together with the absorption spectrum of the BEM core and ωFQFμ shell. Spectra are normalized with respect to the maximum absorption of the ωFQFμ shell. The spherical shell spectrum shows a high-intensity peak centered at 3.24 eV and a low-intensity peak at 3.68 eV. These two peaks can be assigned to the bonding ($|\omega_{s+}\rangle$) and anti-bonding ($|\omega_{s-}\rangle$) plasmonic modes, respectively [see Fig. 2(d)], which are typical of plasmonic nanoshells.[24,100–102] A single plasmonic peak at about 3.43 eV ($|\omega_c\rangle$) is instead present in the spectrum of the BEM core. Such a band corresponds to the dipolar plasmonic excitation [see Fig. 2(d)].

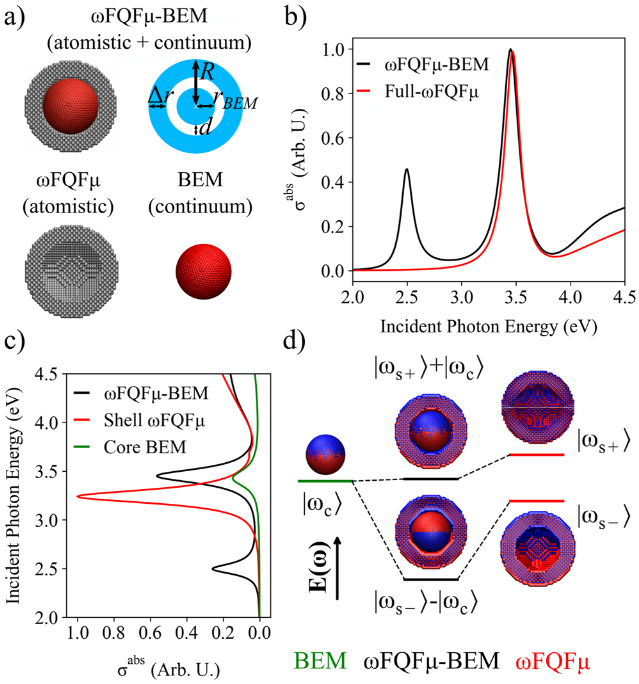

FIG. 2. (a) Graphical representation and geometrical parameters of a spherical NP described by ωFQFμ-BEM. (b) Normalized absorption cross sections σ^{abs} of a spherical Ag NP (radius = 40 Å) computed at the ωFQFμ-BEM and full-ωFQFμ levels. (c) Normalized absorption spectra of the selected spherical NP calculated at the ωFQFμ-BEM level, together with the absorption spectra of the BEM core and ωFQFμ shell. See panel (a). (d) Schematic picture of the hybridization of BEM charge distribution (left) and ωFQFμ densities (right), leading to ωFQFμ-BEM charges and densities (center) calculated at the corresponding PRFs.

The two peaks reported in the ωFQFμ-BEM spectrum of the spherical NP are thus due to the hybridization of isolated plasmonic modes from the core and shell, similar to what has been reported for other nanostructures.[102–106] More specifically, the ωFQFμ-BEM peak at 2.50 eV is associated with the hybrid $|\omega_{s-}\rangle - |\omega_c\rangle$ mode, while the band centered at 3.45 eV corresponds to the $|\omega_{s+}\rangle + |\omega_c\rangle$ mode combination [see Fig. 2(d)]. The presence of the low-energy peak is not unexpected because the approach discards any charge transfer between the two classical regions. This peak thus arises as an artifact of our model. However, it can be easily identified because it will always be the lowest energy peak computed in the spectrum (without the need for any benchmarking with a reference calculation), as predicted by hybridization theory.[102,105] In the following, the focus will thus shift to the $|\omega_{s+}\rangle + |\omega_c\rangle$ band, whose PRF remarkably aligns with that predicted at the full-ωFQFμ level. For clarity, Fig. S1 of the supplementary material presents a comparison between the densities computed from the charges + dipoles distribution of the ωFQFμ-BEM $|\omega_{s+}\rangle + |\omega_c\rangle$ band and the full-ωFQFμ PRF, illustrating a clear one-to-one correspondence.

As a final remark, a third $|\omega_{s+}\rangle - |\omega_c\rangle$ mode arises from the hybridization of plasmonic modes. However, the small dipole moment associated with this mode makes it undetectable in the spectra.[102,105] Moreover, the relative intensities of the $|\omega_{s-}\rangle - |\omega_c\rangle$ and $|\omega_{s+}\rangle + |\omega_c\rangle$ modes are consistent with the expected hybridization behavior. In particular, the stronger intensity of the $|\omega_{s+}\rangle + |\omega_c\rangle$ mode is expected due to the in-phase oscillation of the core and shell dipole moments.[102,105]

2. Plasmonic response dependence on the thickness of the atomistic shell

This section first examines how a variation in the shell thickness and core–shell distance d influences the optical response of the metal NPs. In particular, the shell thickness Δr varies from 13.98 to 7.93 Å, with a constant step of ~2.0 Å. Two core-to-shell distances are considered: $d = 2.88$ Å and $d = 5.76$ Å, corresponding to integer multiples of the nearest neighbor distance (2.88 Å) in the studied FCC lattice. In all cases, the BEM matrix is described by the Brendel–Bormann dielectric function.[93]

Figures 3(a)–3(c) reports absorption cross sections of the spherical NP as a function of shell thickness Δr for $d = 2.88$ and $d = 5.76$ Å, respectively. Data are normalized with respect to the full-ωFQFμ PRF absorption. As a reference, the normalized absorption spectrum computed at the full-ωFQFμ level is reported in all panels. All ωFQFμ-BEM spectra feature an intense peak in the region 3.0–4.5 eV. Such a peak is associated with a dipolar plasmon, as commented in Sec. IV A 1. ωFQFμ-BEM computed PRFs remain almost constant as a function of the shell thickness and only present slight shifts of 0.02–0.04 eV with respect to ωFQFμ PRF (3.47 eV), regardless of the value of d. Differently, reducing the shell thickness systematically increases the absorption intensity mismatch at the PRF between ωFQFμ-BEM and the reference ωFQFμ data. Notably, the mismatch becomes more pronounced for structures with $d = 2.88$ Å. This behavior is probably due to numerical instabilities occurring when solving the ωFQFμ-BEM linear equation [see Eq. (14)] for the smaller d values, associated with the so-called polarization catastrophe raising for the increase of electrostatic/polarization interactions.[107]

To further analyze the plasmonic response as a function of d, Figs. 3(b) and 3(d) graphically illustrate the differences in the computed charges + dipoles density at the ωFQFμ-BEM and full-ωFQFμ levels. In all cases, densities are computed at the PRF for $d = 2.88$ Å and $d = 5.76$ Å, respectively. This qualitative analysis permits us to evaluate the charges + dipoles density deviation near the NP surface of ωFQFμ-BEM with respect to the full-ωFQFμ atomistic structure, whose surface is graphically represented by green dots. The most remarkable differences are observed at the core region, and in particular at the BEM-ωFQFμ interface. This is expected and is due to the artificial boundary that is introduced in our multiscale method. However, since we are dealing with localized surface plasmons, we are particularly interested in a proper description of surface properties. Note that the differences at the NP surface are negligible for all methods, thus validating the novel methodology. The agreement between the two methods worsens by reducing the atomistic shell thickness, especially for $d = 2.88$ Å. This is again related to numerical instabilities in solving the ωFQFμ-BEM linear equation.

For a more quantitative analysis of the plasmonic density differences close to the NP, in Table I, computed relative errors (ρ^{error}) between integrated densities of ωFQFμ-BEM and full-ωFQFμ are collected. Values are calculated at their corresponding PRFs. ρ^{error} is evaluated within a volume V close to the NP surface, defined as a three-dimensional parallelogram constrained by the coordinate ranges $x, z \in [-10, 10]$ Å and $y \in [40, 50]$ Å (see Fig. S2 of

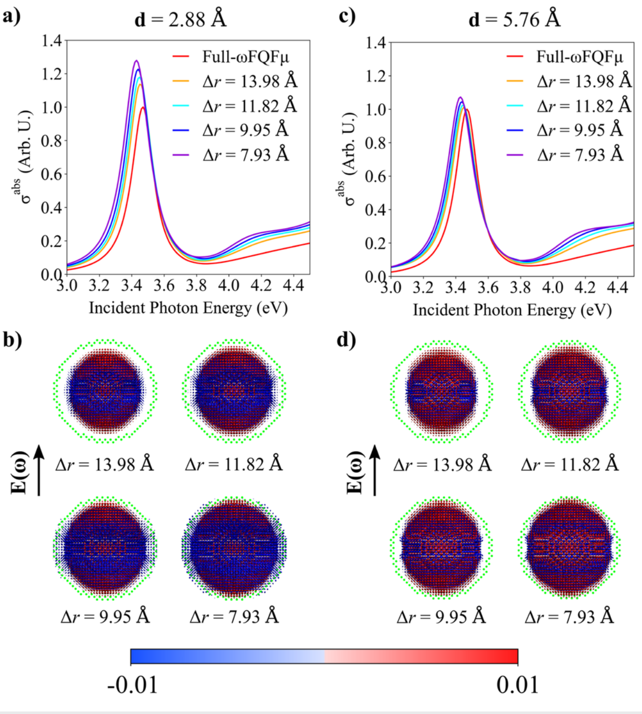

FIG. 3. Normalized absorption spectra of a spherical NP (a) and (c) and absolute density differences plots calculated at the PRFs [(b) and (d) green dots represent surface NP atoms] as a function of Δr. The NP is described at the full-ωFQFμ and ωFQFμ-BEM levels, setting $d = 2.88$ Å (a) and (b) and $d = 5.76$ Å (c) and (d).

TABLE I. PRFs of the studied spherical NP ($R = 40$ Å) calculated at the ωFQFμ-BEM level ($d = 2.88$ Å and $d = 5.76$ Å) as a function of geometrical parameters (Δr, N_{Atoms}, r_{BEM}). ωFQFμ-BEM computational % speed-up and ρ^{error} with respect to full-ωFQFμ reference are also given.

Δr (Å)	N_{Atoms}	r_{BEM} (Å)	PRF (eV)	Speed-up (%)	ρ^{error} (%)
		$d = 2.88$ Å			
13.98	11 470	23.14	3.45	44.35	11.74
11.82	10 258	25.30	3.45	56.87	14.36
9.95	9 080	27.17	3.44	66.01	19.34
7.93	7 676	29.19	3.43	77.32	21.25
		$d = 5.76$ Å			
13.98	11 470	20.26	3.45	42.56	3.49
11.82	10 258	22.42	3.44	53.55	5.45
9.95	9 080	24.29	3.44	65.20	6.77
7.93	7 676	26.31	3.43	75.81	10.42
Full-ωFQFμ	15 683	—	3.47	—	—

the supplementary material for a graphical representation). ρ^{error} is calculated as follows:

$$\rho^{\text{error}} = \frac{\int_V |\rho_{\text{PRF}}^{\omega\text{FQF}\mu-\text{BEM}}(\mathbf{r}) - \rho_{\text{PRF}}^{\text{Full}-\omega\text{FQF}\mu}(\mathbf{r})|\mathbf{dr}^3}{\int_V |\rho_{\text{PRF}}^{\text{Full}-\omega\text{FQF}\mu}(\mathbf{r})|\mathbf{dr}} \cdot 100, \tag{24}$$

where $\rho_{\text{PRF}}^{\omega\text{FQF}\mu-\text{BEM}}$ and $\rho_{\text{PRF}}^{\text{Full}-\omega\text{FQF}\mu}$ are the ωFQFμ-BEM and full-ωFQFμ densities calculated at their PRF, respectively. The results reported in Table I confirm the qualitative behavior depicted in Fig. 3. In fact, by decreasing the shell thickness, the computed ρ^{error} values increase for both d = 2.88 Å (ranging from about 12% to about 21%) and d = 5.76 Å (ranging from about 3% to about 10%). In addition, this quantitative analysis confirms the better numerical performance of the ωFQFμ-BEM structures with d = 5.76 Å, which are consistently associated with the lowest relative errors. Remarkably, for the largest Δr, ωFQFμ-BEM is associated with a relative error of about 3%, thus validating our novel approach as compared to a full atomistic description.

To conclude this section, we investigate the computational savings associated with the multiscale ωFQFμ-BEM as compared to a full ωFQFμ description of the spherical NP. To this end, the relative computational speed-up (in percentage) for single-frequency calculations (at the PRF of the systems) is reported in Table I as a function of d and Δr. We remark that all calculations exploit a constant number of *tesserae* to mesh the BEM core (~2980 *tesserae*). The data reported in Table I clearly show a substantial computational saving, ranging from about 43% to about 77%, independent of d for a given value or Δr. This is expected because the number of atoms in the ωFQFμ shell decreases while the number of *tesserae* representing the BEM core remains constant. It is worth remarking that for the most accurate ωFQFμ-BEM partitioning (Δr = 13.98 Å, d = 5.76 Å), the speed-up of ωFQFμ-BEM is considerable, without losing accuracy as compared to a full ωFQFμ description. Therefore, the above model parameters represent the best compromise between accuracy and computational cost for ωFQFμ-BEM applications.

3. Plasmonic response dependence on the BEM dielectric functions

We now move to analyze the model parameters affecting the BEM core response, namely, the dielectric function and the number of *tesserae*. To this end, we consider three dielectric functions that are commonly exploited to describe Ag response, recovered from Brendel–Bormann (BB),[93] Palik,[92] and Johnson and Christy (J & C).[94] Computed absorption cross sections for the selected spherical NP exploiting the three permittivity functions are normalized with respect to the full-ωFQFμ reference and graphically depicted in Figs. 4(a)–4(c), for d = 5.76 Å (see Fig. S3 of the supplementary material for additional values obtained with d = 2.88 Å). Absorption properties are reported as a function of the shell thickness Δr. The normalized full atomistic ωFQFμ absorption spectrum is also shown as a reference.

All computed spectra are characterized by a main plasmonic peak, which is associated with a dipolar localized surface plasmon. ωFQFμ-BEM computed PRFs (see also Table II) remain constant as a function of the shell thickness by exploiting Palik and J & C permittivity functions (3.48 eV), and remarkably the computed PRF is shifted by only 0.01 eV with respect to the reference ωFQFμ PRF (3.47 eV). As commented in Sec. IV A 2, by using the BB $\varepsilon(\omega)$, the PRF slightly shifts by decreasing the shell thickness (from 3.45 eV–Δr = 13.98 Å to 3.43 eV–Δr = 7.93 Å). However, also in this case, all data agree with the reference ωFQFμ PRF within the chemical accuracy (0.04 eV to 0.9 kcal/mol).

The absorption cross section at the PRF varies significantly depending on the chosen dielectric function. Notably, absorption intensities in very good agreement with the reference ωFQFμ model are obtained by employing BB and Palik dielectric functions. The ωFQFμ-BEM spectrum computed by using the Palik dielectric function presents a small shoulder at about 3.3 eV, which is also observed at the full BEM level (see Fig. S4 in the supplementary material) and is thus related to the use of this specific permittivity function. In contrast, a pronounced intensity mismatch as compared to the full-ωFQFμ absorption curve is observed if the J & C dielectric function is employed. Remarkably, such a discrepancy increases as the shell thickness decreases.

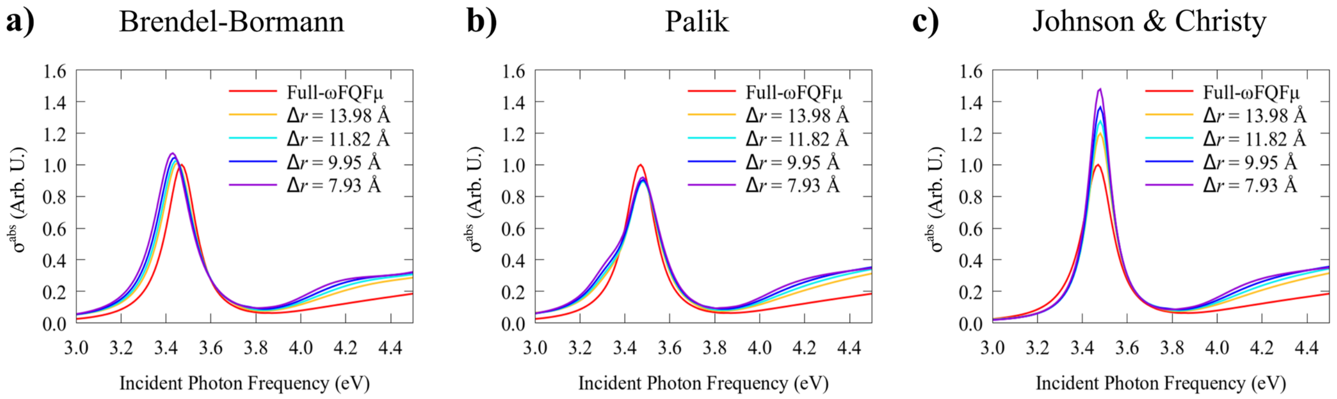

FIG. 4. Normalized absorption spectra of a spherical Ag NP (R = 40 Å) treated at the ωFQFμ-BEM (d = 5.76 Å) levels as a function of Δr and BEM dielectric function [Brendel–Bormann (a), Palik (b), and Johnson and Christy (c)]. Full-ωFQFμ spectra are also depicted as a reference.

TABLE II. PRFs and ρ^{error} computed for the studied spherical Ag NP (R = 40 Å) at the full-ωFQFμ and ωFQFμ-BEM (d = 5.76 Å) levels, as a function of ωFQFμ-BEM geometrical parameter Δr and BEM dielectric function [Brendel–Bormann (BB), Palik, and Johnson and Christy (J & C)].

Δr (Å)	Dielectric function	PRF (eV)	ρ^{error} (%)
13.98	BB	3.45	3.49
	Palik	3.48	8.21
	J & C	3.48	22.21
11.82	BB	3.44	5.45
	Palik	3.48	9.26
	J & C	3.48	28.30
9.95	BB	3.44	6.77
	Palik	3.48	10.70
	J & C	3.48	31.82
7.93	BB	3.43	10.42
	Palik	3.48	9.22
	J & C	3.48	44.45
Full-ωFQFμ	—	3.47	—

To quantitatively analyze surface-related near-field properties, ρ^{error} values as a function of the permittivity function and Δr are reported in Table II. Computed relative errors using BB and J & C permittivities consistently increase by reducing the atomistic shell thickness, unlike those obtained by exploiting the Palik dielectric function, which remains almost constant (about 9%). Notably, the best results (i.e., lowest errors) are obtained by employing BB, with the exception of the case Δr = 7.93 Å for which Palik gives the best results. J & C data substantially deviate from reference ωFQFμ values. On the other hand, BB emerges as the most robust permittivity function model to exploit in ωFQFμ-BEM applications.

As a final validation, we investigate the dependence of absorption spectra on the number of *tesserae* used to mesh the BEM core. In particular, we consider four different tessellations of the spherical BEM core (2990, 1948, 1018, and 390 *tesserae*), while keeping the other model parameters fixed to the best set resulting from the previous analysis (d = 5.76 Å, Δr = 13.98 Å, BB permittivity function). Numerical results are reported in Fig. S5 and Table S3 of the supplementary material. Interestingly, the discretization of the core only minimally affects the plasmonic response (spectra, density-differences plots, and ρ^{error}), while yielding substantial computational % speed-ups, up to 56.68% for 390 *tesserae*. To conclude, the best parameter set, which guarantees the best compromise between computational cost and accuracy, is defined by d = 5.76 Å, Δr = 13.98 Å, the BB permittivity function, and 390 *tesserae*.

B. Molecular plasmonics: QM/ωFQFμ-BEM for SERS

As mentioned in Sec. I and specified in Sec. II B, ωFQFμ-BEM can be coupled to a QM Hamiltonian in a QM/Classical fashion and extended to compute SERS spectra. This section showcases the potentialities of the method to compute SERS spectra of pyridine near the tip of complex-shaped NPs. To this end, Ag icosahedral (Ih) NPs of increasing size (from 1.9 to 3.8 nm) are selected, and additional calculations modeling the molecule–NP system at the fully atomistic (QM/ωFQFμ) and fully implicit (QM/BEM) levels are discussed. A graphical representation highlighting the structural differences between the various methods is given in Fig. 5, panel (a), whereas geometrical parameters are shown in Table S4 in the supplementary material. To fully characterize ωFQFμ-BEM Ih systems and, similarly, spherical NPs, four parameters are exploited (the BEM radius r_{BEM}, the BEM-ωFQFμ distance d, the average thickness of the ωFQFμ shell Δr, and the NP radius R), while the equivalent full-ωFQFμ and full-BEM structures are described by a single radius parameter (R). Detailed data on the geometrical features and PRFs of the systems are gathered in Tables S4–S6 of the supplementary material.

In Fig. 5, the SERS signal of pyridine on Ag Ih NPs is studied as a function of the NP radius. Pyridine is adsorbed perpendicularly to the NP surface at a distance of 3 Å, with the N atom lying closest to the NP. In agreement with the preliminary analysis in Sec. IV A, the BB dielectric function is employed, and d is set to 5.76 Å. Figure 5(b) illustrates SERS intensities as a function of the NP radius, normalized with respect to the largest signal exhibited by each model. In all cases, this corresponds to the SERS signal of pyridine interacting with the largest Ih NP. Notably, for all models, only the signals associated with specific normal modes are enhanced (see Fig. S7 in the supplementary material for their graphical depiction). This is due to the fact that such vibrations are related to an orthogonal movement of pyridine atoms with respect to the NP surface. As a consequence, they experience the largest field gradient variation and are, therefore, preferentially enhanced, as has recently been shown by some of us.[11] The analysis of the results reveals significant similarities between the QM/ωFQFμ-BEM and QM/ωFQFμ approaches while also highlighting substantial discrepancies by using QM/BEM. In particular, the observed Raman peaks are consistent across all models when pyridine is adsorbed on the largest NPs (radius >2.7 nm). On the contrary, the smallest full-BEM structures (radius <2.5 nm) substantially deviate from the full atomistic picture [see Fig. 5(b)]. To better compare the three approaches, Fig. 5(c) presents normalized Raman spectra for the largest NP studied using each theoretical framework. The spectra depicted in Fig. 5(c) show an almost perfect alignment of the relative Raman intensities between ωFQFμ-BEM and full-ωFQFμ NPs. In contrast, substantial discrepancies are evident for full-BEM structures, particularly for the Raman peaks centered at 1024, 1207, 1460, and 1568 cm^{-1}.

To comprehensively analyze the performance of the various models, Fig. 5(d) collects AEF and MEF descriptors calculated as a function of the NP radius. For all methods, such indices are monotonically increasing. The reference QM/ωFQFμ approach predicts a maximum AEF and MEF of about 5000 and 12 000, respectively, thus displaying an overall enhancement of about 10^3. QM/BEM shows a substantial quantitative mismatch, providing AEF and MEF that are completely overestimated by several orders of magnitude (about 10^8). Conversely, QM/ωFQFμ-BEM presents a clear trend of quantitative similarity with the reference fully atomistic results, predicts AEF and MEF of the same order of magnitude, and only deviates from the reference by a factor of about 1.35 for the largest structure. In addition, in Fig. S8 of the supplementary material, normalized gas-phase Raman and SERS spectra computed

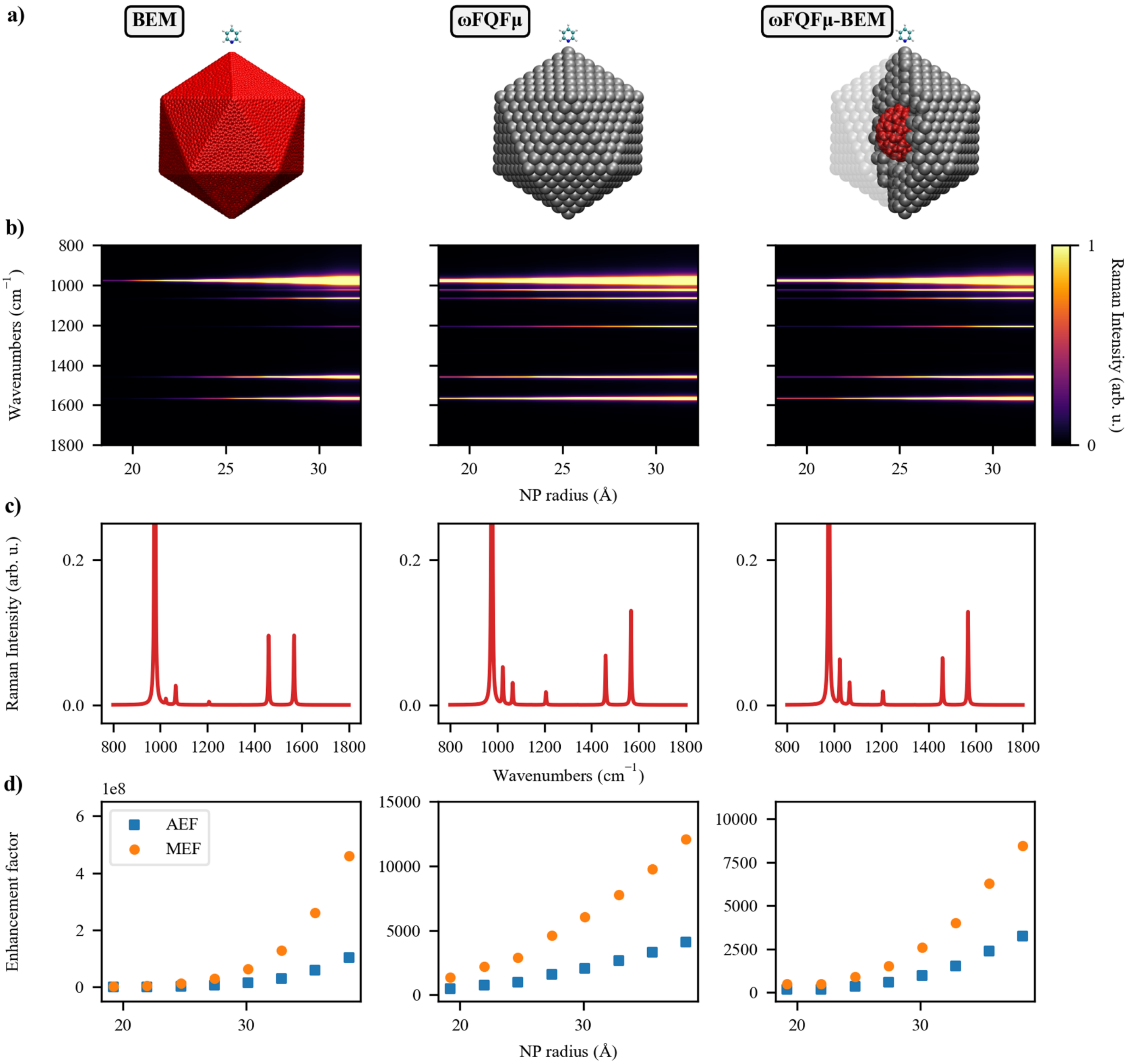

FIG. 5. Graphical depiction of pyridine adsorbed on Ag Ih systems described at the full-BEM (left), full-ωFQFμ (center), and ωFQFμ-BEM (right) levels. (b) Normalized pyridine SERS spectra as a function of the NP radius. (c) Normalized SERS of pyridine adsorbed on the largest NP. (d) AEF and MEF as a function of the NP radius. BEM response is described with the BB dielectric function, and ωFQFμ-BEM Ih systems are characterized by d = 5.76 Å.

at PRF are reported for the largest nanoparticle studied using each formalism.

It is worth remarking that the QM/BEM trends arising from Fig. 5 can be substantially affected by varying the dielectric functions (J & C and Palik). These results are reported in Sec. S2.3 of the supplementary material and show that J & C permittivity yields a complete modification of the spectral response for the largest NP (see Figs. S9 and S12 of the supplementary material), also affecting computed AEF and MEF values, further magnifying the quantitative discrepancies compared to the fully atomistic ωFQFμ description. Conversely, the QM/ωFQFμ-BEM spectra remain consistent regardless of the chosen parameters but are crucially affected by a variation in the BEM-ωFQFμ distance d. In fact, by setting $d = 2.88$ Å, inconsistent trends in both AEF and MEF are reported as the system size increases (see Figs. S11–S13 of the supplementary material). This behavior completely aligns with our findings from the study on ρ^{error} of spherical ωFQFμ-BEM NPs (see Sec. IV A).

To remove any arbitrariness in selecting the minimum NP-pyridine distance for the full-BEM systems, we have performed distance-dependent studies of AEF and MEF for pyridine adsorbed on the tip of icosahedral nanoparticles with a 3 nm radius. These calculations were performed at the full-BEM, full-ωFQFμ, and ωFQFμ-BEM (characterized by the BB dielectric function and $d = 5.76$ Å) levels, as shown in Fig. S14 in the supplementary material. The results reveal a monotonic decrease in both descriptors for all three models, supporting the validity of our full-BEM calculations. In addition, the decay trends for full-ωFQFμ and ωFQFμ-BEM show a one-to-one correspondence, while the full-BEM studies exhibit a smoother decay with distance, further corroborating the robustness of the ωFQFμ-BEM approach.

We conclude this section by remarking on the enhanced computational efficiency of the QM/ωFQFμ-BEM method as compared to the fully atomistic ωFQFμ description (see Table S7 of the supplementary material for the numerical % speed-up). Notably, the computational saving is particularly evident for the largest systems (radius >3 nm), for which, as previously discussed, an improved quantitative and qualitative description of the SERS response is also obtained. These findings underscore the potential of ωFQFμ-BEM for its application to large systems, where atomistic details at their surface play a major role in their plasmonic features, offering a substantial reduction in computational cost, up to 58%.

V. CONCLUSIONS

This work has presented a novel multiscale implicit–atomistic approach (ωFQFμ-BEM) to investigate the plasmonic response of metal NPs. ωFQFμ-BEM combines a spherical implicit continuum core embedded within an atomistically defined shell, preserving the essential plasmonic response at the NP surface. The method is theoretically constructed by integrating the fully atomistic ωFQFμ and implicit BEM methodologies for plasmonics and constitutes the first attempt to merge atomistic and continuum descriptions for the study of plasmonic substrates in the context of classical electrodynamics. To validate the ωFQFμ-BEM model, we have initially demonstrated its capacity to reproduce the absorption cross section of spherical Ag nanoparticles, taking the fully atomistic ωFQFμ method as a reference. In particular, we have presented a comprehensive analysis of the different factors influencing ωFQFμ-BEM response: the thickness of the atomistic shell, BEM-ωFQFμ distance, BEM dielectric function, and discretization of the continuum core. Our in-depth analysis suggests that the best results at the implicit continuum–atomistic ωFQFμ-BEM level for Ag NPs are obtained by setting the BEM-ωFQFμ distance to twice the nearest neighbor distance and using the Brendel–Bormann dielectric function while keeping the outer shells described atomistically.

The coupling of ωFQFμ-BEM to a QM region has been presented, giving rise to the QM/ωFQFμ-BEM approach, which is able to describe molecular plasmonics, i.e., how plasmons affect the molecular electronic structure and the resulting spectral signals. To showcase the potentialities of the method, QM/ωFQFμ-BEM has been challenged to reproduce the SERS response of pyridine adsorbed on the tip of Ag Ih NPs. The quality of the method has been assessed by an in-depth comparison with fully atomistic QM/ωFQFμ (reference) and fully implicit QM/BEM spectra. Our results show that, while QM/BEM outcomes strongly differ, QM/ωFQFμ-BEM can reproduce QM/ωFQFμ SERS spectra, specifically for the largest NP sizes. More in detail, an almost perfect agreement of normalized Raman intensities for the largest system is observed, along with a similar qualitative and quantitative outcome for AEF and MEF descriptors with increasing NP radius. As a result of this work, two main points may be highlighted: (i) an implicit description of the NP structure yields substantial discrepancies in simulated SERS spectra as compared to an atomistic description and should be generally avoided; and (ii) it is crucial to describe at a full atomistic level the NP surface, while the core can be safely treated by an implicit description. Finally, the enhanced computational efficiency observed for the largest QM/ωFQFμ-BEM structures yields a computational saving of more than half compared to QM/ωFQFμ. Therefore, large, complex-shaped systems can be afforded. This originates from a substantial reduction of the computational effort required to solve the linear system in Eq. (14), whose dimension is strongly reduced by replacing the core atoms with a continuum description. In addition, memory-related issues are mitigated. To end the presentation, it is worth mentioning that both BEM and ωFQFμ models are formulated in the quasistatic regime, i.e., retardation effects are discarded. Therefore, they appropriately treat systems of dimension significantly smaller than that of the incident wavelength. In addition, in ωFQFμ-BEM, the ωFQFμ and BEM layers interact via electrostatic forces, i.e., charge transfer is inhibited. The above two limitations of the approach will deserve careful investigation in future communications.

SUPPLEMENTARY MATERIAL

See the supplementary material for details on ωFQFμ-BEM equations. Geometrical parameters, PRFs, ρ^{error}, and computational speed-ups. Defined volume for ρ^{error} calculations. Further results on classical and QM/classical responses as a function of core-to-shell distance, dielectric function, and BEM core discretization for spherical and Ih core–shell systems. Graphical representation of pyridine's normal modes.

ACKNOWLEDGMENTS

The authors acknowledge Professor Stefano Corni (University of Padova) for the fruitful discussions. We gratefully acknowledge the Center for High-Performance Computing (CHPC) at SNS for providing the computational infrastructure. This work has received funding from the European Research Council (ERC) under the European Union's Horizon 2020 research and innovation program (Grant Agreement No. 818064).

AUTHOR DECLARATIONS

Conflict of Interest

The authors have no conflicts to disclose.

Author Contributions

Pablo Grobas Illobre: Data curation (lead); Formal analysis (lead); Investigation (lead); Methodology (equal); Software (lead); Validation (lead); Visualization (lead); Writing – original draft (lead). **Piero Lafiosca**: Software (supporting). **Luca Bonatti**: Methodology (equal); Software (supporting). **Tommaso Giovannini**: Conceptualization (equal); Formal analysis (equal); Investigation (equal); Methodology (equal); Writing – original draft (equal); Writing – review & editing (equal). **Chiara Cappelli**: Conceptualization (equal); Funding acquisition (lead); Project administration (lead); Resources (lead); Supervision (lead); Writing – review & editing (equal).

DATA AVAILABILITY

The data that support the findings of this study are available from the corresponding author upon reasonable request.

REFERENCES

[1] V. Giannini, A. I. Fernández-Domínguez, S. C. Heck, and S. A. Maier, Chem. Rev. **111**, 3888 (2011).

[2] S. A. Maier, *Plasmonics: Fundamentals and Applications* (Springer Science & Business Media, 2007).

[3] T. W. Odom and G. C. Schatz, "Introduction to plasmonics," Chem. Rev. **111**, 3667 (2011).

[4] K. L. Kelly, E. Coronado, L. L. Zhao, and G. C. Schatz, "The optical properties of metal nanoparticles: The influence of size, shape, and dielectric environment," J. Phys. Chem. B **107**, 668 (2003).

[5] E. Coccia, J. Fregoni, C. Guido, M. Marsili, S. Pipolo, and S. Corni, J. Chem. Phys. **153**, 200901 (2020).

[6] K. A. Willets and R. P. Van Duyne, Annu. Rev. Phys. Chem. **58**, 267 (2007).

[7] R. Zhang, Y. Zhang, Z. Dong, S. Jiang, C. Zhang, L. Chen, L. Zhang, Y. Liao, J. Aizpurua, Y. e. Luo *et al.*, Nature **498**, 82 (2013).

[8] S. Jiang, Y. Zhang, R. Zhang, C. Hu, M. Liao, Y. Luo, J. Yang, Z. Dong, and J. Hou, Nat. Nanotechnol. **10**, 865 (2015).

[9] N. Chiang, X. Chen, G. Goubert, D. V. Chulhai, X. Chen, E. A. Pozzi, N. Jiang, M. C. Hersam, T. Seideman, L. Jensen, and R. P. Van Duyne, Nano Lett. **16**, 7774 (2016).

[10] J. Langer, D. Jimenez de Aberasturi, J. Aizpurua, R. A. Alvarez-Puebla, B. Auguié, J. J. Baumberg, G. C. Bazan, S. E. Bell, A. Boisen, A. G. Brolo *et al.*, ACS Nano **14**, 28 (2019).

[11] P. Lafiosca, L. Nicoli, L. Bonatti, T. Giovannini, S. Corni, and C. Cappelli, J. Chem. Theory Comput. **19**, 3616 (2023).

[12] L. Zhao, L. Jensen, and G. C. Schatz, J. Am. Chem. Soc. **128**, 2911 (2006).

[13] L. Jensen, C. M. Aikens, and G. C. Schatz, Chem. Soc. Rev. **37**, 1061 (2008).

[14] S. M. Morton and L. Jensen, J. Am. Chem. Soc. **131**, 4090 (2009).

[15] S. M. Morton, D. W. Silverstein, and L. Jensen, Chem. Rev. **111**, 3962 (2011).

[16] A. Sanchez-Gonzalez, S. Corni, and B. Mennucci, J. Phys. Chem. C **115**, 5450 (2011).

[17] S. M. Morton and L. Jensen, J. Chem. Phys. **133**, 074103 (2010).

[18] S. M. Morton and L. Jensen, J. Chem. Phys. **135**, 134103 (2011).

[19] G. Mie, Ann. Phys. **330**, 377 (1908).

[20] A. Taflove, S. C. Hagness, and M. Piket-May, *Computational Electromagnetics: The Finite-Difference Time-Domain Method* (Elsevier, Amsterdam, The Netherlands, 2005).

[21] F. J. García de Abajo and A. Howie, Phys. Rev. B **65**, 115418 (2002).

[22] V. Myroshnychenko, E. Carbó-Argibay, I. Pastoriza-Santos, J. Pérez-Juste, L. M. Liz-Marzán, and F. J. García de Abajo, Adv. Mater. **20**, 4288 (2008).

[23] B. Mennucci and S. Corni, Nat. Rev. Chem. **3**, 315 (2019).

[24] L. Bonatti, G. Gil, T. Giovannini, S. Corni, and C. Cappelli, Front. Chem. **8**, 340 (2020).

[25] L. L. Jensen and L. Jensen, J. Phys. Chem. C **112**, 15697 (2008).

[26] L. L. Jensen and L. Jensen, J. Phys. Chem. C **113**, 15182 (2009).

[27] V. I. Zakomirnyi, Z. Rinkevicius, G. V. Baryshnikov, L. K. Sørensen, and H. Ågren, J. Phys. Chem. C **123**, 28867 (2019).

[28] V. I. Zakomirnyi, I. L. Rasskazov, L. K. Sørensen, P. S. Carney, Z. Rinkevicius, and H. Ågren, Phys. Chem. Chem. Phys. **22**, 13467 (2020).

[29] J. L. Payton, S. M. Morton, J. E. Moore, and L. Jensen, J. Chem. Phys. **136**, 214103 (2012).

[30] Z. Pei, Y. Mao, Y. Shao, and W. Liang, J. Chem. Phys. **157**, 164110 (2022).

[31] T. Giovannini, M. Rosa, S. Corni, and C. Cappelli, Nanoscale **11**, 6004 (2019).

[32] T. Giovannini, L. Bonatti, M. Polini, and C. Cappelli, J. Phys. Chem. Lett. **11**, 7595 (2020).

[33] P. Lafiosca, T. Giovannini, M. Benzi, and C. Cappelli, J. Phys. Chem. C **125**, 23848 (2021).

[34] L. Bonatti, L. Nicoli, T. Giovannini, and C. Cappelli, Nanoscale Adv. **4**, 2294 (2022).

[35] T. Giovannini, L. Bonatti, P. Lafiosca, L. Nicoli, M. Castagnola, P. G. Illobre, S. Corni, and C. Cappelli, ACS Photonics **9**, 3025 (2022).

[36] S. Zanotto, L. Bonatti, M. F. Pantano, V. Mišeikis, G. Speranza, T. Giovannini, C. Coletti, C. Cappelli, A. Tredicucci, and A. Toncelli, ACS Photonics **10**, 394 (2023).

[37] L. Nicoli, P. Lafiosca, P. Grobas Illobre, L. Bonatti, T. Giovannini, and C. Cappelli, Front. Photonics **4**, 1199598 (2023).

[38] P. Lafiosca, L. Nicoli, S. Pipolo, S. Corni, T. Giovannini, and C. Cappelli, J. Phys. Chem. C **128**, 17513 (2024).

[39] L. Nicoli, S. Sodomaco, P. Lafiosca, T. Giovannini, and C. Cappelli, ACS Phys. Chem. Au **4**, 669 (2024).

[40] S. Corni and J. Tomasi, J. Chem. Phys. **114**, 3739 (2001).

[41] S. Corni and J. Tomasi, Chem. Phys. Lett. **342**, 135 (2001).

[42] S. Corni and J. Tomasi, J. Chem. Phys. **116**, 1156 (2002).

[43] S. Corni and J. Tomasi, Chem. Phys. Lett. **365**, 552 (2002).

[44] S. Corni and J. Tomasi, *Surface-Enhanced Raman Scattering* (Springer, 2006), pp. 105–123.

[45] M. Romanelli, G. Dall'Osto, and S. Corni, J. Chem. Phys. **155**, 214304 (2021).

[46] C. V. Coane, M. Romanelli, G. Dall'Osto, R. Di Felice, and S. Corni, Commun. Chem. **7**, 32 (2024).

[47] U. Hohenester and A. Trügler, Comput. Phys. Commun. **183**, 370 (2012).

[48] M. E. Casida, *Recent Advances in Density Functional Methods: (Part I)* (World Scientific, 1995), pp. 155–192.

[49] M. G. Albrecht and J. A. Creighton, J. Am. Chem. Soc. **99**, 5215 (1977).

[50] D. L. Jeanmaire and R. P. Van Duyne, J. Electroanal. Chem. Interfacial Electrochem. **84**, 1 (1977).

[51] A. Campion and P. Kambhampati, Chem. Soc. Rev. **27**, 241 (1998).

[52] C. E. Talley, J. B. Jackson, C. Oubre, N. K. Grady, C. W. Hollars, S. M. Lane, T. R. Huser, P. J. Nordlander, and N. J. Halas, Nano Lett. **5**(8), 1569 (2005).

[53] R. Alvarez-Puebla, L. M. Liz-Marzán, and F. J. García de Abajo, J. Phys. Chem. Lett. **1**, 2428 (2010).

[54] E. Le Ru and P. Etchegoin, *Principles of Surface-Enhanced Raman Spectroscopy: And Related Plasmonic Effects* (Elsevier, 2008).

[55] B. Sharma, R. R. Frontiera, A.-I. Henry, E. Ringe, and R. P. Van Duyne, Mater. Today **15**, 16 (2012).

[56] X. X. Han, R. S. Rodriguez, C. L. Haynes, Y. Ozaki, and B. Zhao, Nat. Rev. Methods Primers **1**, 87 (2022).

[57] J. T. Golab, J. R. Sprague, K. T. Carron, G. C. Schatz, and R. P. Van Duyne, J. Chem. Phys. **88**, 7942 (1988).

[58] H. Lai, F. Xu, Y. Zhang, and L. Wang, J. Mater. Chem. B **6**, 4008 (2018).

[59] H. Zhang, S. Duan, P. M. Radjenovic, Z.-Q. Tian, and J.-F. Li, Acc. Chem. Res. **53**, 729 (2020).

[60] H.-S. Su, H.-S. Feng, X. Wu, J.-J. Sun, and B. Ren, Nanoscale **13**(33), 13962 (2021).

[61] X. Zhao, S. Campbell, G. Q. Wallace, A. Claing, C. G. Bazuin, and J.-F. Masson, ACS Sens. **5**, 2155 (2020).

[62] L. Fang, X.-T. Pan, K. Liu, D. Jiang, D. Ye, L.-N. Ji, K. Wang, and X. Xia, ACS Appl. Mater. Interfaces **15**, 20677 (2023).
[63] L. Troncoso-Afonso, G. A. Vinnacombe-Willson, C. García-Astrain, and L. M. Liz-Marzán, Chem. Soc. Rev. **53**, 5118 (2024).
[64] J. Perumal, Y. Wang, A. B. E. Attia, U. S. Dinish, and M. Olivo, Nanoscale **13**, 553 (2021).
[65] R. Taheri-Ledari, F. Ganjali, S. Zarei-Shokat, R. Dinmohammadi, F. R. Asl, A. Emami, Z. Mojtabapour, Z. Rashvandi, A. Kashtiaray, F. Jalali, and A. Maleki, Nanoscale Adv. **5**, 6768 (2023).
[66] A. Pinchuk, G. v. Plessen, and U. Kreibig, J. Phys. D: Appl. Phys. **37**, 3133 (2004).
[67] A. Pinchuk, U. Kreibig, and A. Hilger, Surf. Sci. **557**, 269 (2004).
[68] B. Balamurugan and T. Maruyama, Appl. Phys. Lett. **87**, 143105 (2005).
[69] T. Giovannini, A. Puglisi, M. Ambrosetti, and C. Cappelli, J. Chem. Theory Comput. **15**, 2233 (2019).
[70] A. Mayer, Phys. Rev. B **75**, 045407 (2007).
[71] R. Fuchs, Phys. Rev. B **11**, 1732 (1975).
[72] J. Tomasi, B. Mennucci, and R. Cammi, Chem. Rev. **105**, 2999 (2005).
[73] S. Vukovic, S. Corni, and B. Mennucci, J. Phys. Chem. C **113**, 121 (2009).
[74] P. Grobas Illobre, P. Lafiosca, T. Guidone, F. Mazza, T. Giovannini, and C. Cappelli, Nanoscale Adv. **6**, 3410 (2024).
[75] T. Helgaker, P. Jørgensen, and J. Olsen, "Molecular integral evaluation," in *Molecular Electronic-Structure Theory* (John Wiley & Sons, Ltd., 2000), Chap. 9, pp. 336–432.
[76] A. Warshel and M. Levitt, J. Mol. Biol. **103**, 227 (1976).
[77] H. Lin and D. G. Truhlar, Theor. Chem. Acc. **117**, 185 (2007).
[78] H. M. Senn and W. Thiel, Angew. Chem., Int. Ed. **48**, 1198 (2009).
[79] C. A. Guido, M. Rosa, R. Cammi, and S. Corni, J. Chem. Phys. **152**, 174114 (2020).
[80] S. Corni, S. Pipolo, and R. Cammi, J. Phys. Chem. A **119**, 5405 (2015).
[81] E. Baerends *et al.*, ADF (version 2020.x), Theoretical Chemistry, Vrije Universiteit, Amsterdam, The Netherlands, 2020, http://www.scm.com.
[82] L. Nicoli, T. Giovannini, and C. Cappelli, J. Chem. Phys. **157**, 214101 (2022).
[83] P. Norman, K. Ruud, and T. Saue, *Principles and Practices of Molecular Properties: Theory, Modeling, and Simulations* (John Wiley & Sons, 2018).
[84] T. Giovannini, F. Egidi, and C. Cappelli, Phys. Chem. Chem. Phys. **22**, 22864 (2020).
[85] L. Jensen, J. Autschbach, and G. C. Schatz, J. Chem. Phys. **122**, 224115 (2005).
[86] J. L. Payton, S. M. Morton, J. E. Moore, and L. Jensen, Acc. Chem. Res. **47**, 88 (2014).
[87] G. Placzek, in *Handbuch der Radiologie*, edited by G. Marx (Akademische Verlagsgesellschaft, Leipzig, 1934).
[88] G. Placzek and E. Teller, Z. Phys. **81**, 209 (1933).
[89] L. Jensen, L. Zhao, J. Autschbach, and G. Schatz, J. Chem. Phys. **123**, 174110 (2005).
[90] A. H. Larsen, J. J. Mortensen, J. Blomqvist, I. E. Castelli, R. Christensen, M. Dułak, J. Friis, M. N. Groves, B. Hammer, C. Hargus, E. D. Hermes, P. C. Jennings, P. B. Jensen, J. Kermode, J. R. Kitchin, E. L. Kolsbjerg, J. Kubal, K. Kaasbjerg, S. Lysgaard, J. B. Maronsson, T. Maxson, T. Olsen, L. Pastewka, A. Peterson, C. Rostgaard, J. Schiøtz, O. Schütt, M. Strange, K. S. Thygesen, T. Vegge, L. Vilhelmsen, M. Walter, Z. Zeng, and K. W. Jacobsen, J. Phys.: Condens. Matter **29**, 273002 (2017).
[91] C. Geuzaine and J.-F. Remacle, Int. J. Numer. Methods Eng. **79**, 1309 (2009).
[92] E. D. Palik, *Handbook of Optical Constants of Solids* (Elsevier, 1997).
[93] A. D. Rakić, A. B. Djurišić, J. M. Elazar, and M. L. Majewski, Appl. Opt. **37**, 5271 (1998).
[94] P. B. Johnson and R.-W. Christy, Phys. Rev. B **6**, 4370 (1972).
[95] S. Van Gisbergen, J. Snijders, and E. Baerends, J. Chem. Phys. **103**, 9347 (1995).
[96] S. Van Gisbergen, J. Snijders, and E. Baerends, Comput. Phys. Commun. **118**, 119 (1999).
[97] L. Fan and T. Ziegler, J. Chem. Phys. **96**, 9005 (1992).
[98] L. Fan and T. Ziegler, J. Phys. Chem. **96**, 6937 (1992).
[99] S. Van Gisbergen, J. Snijders, and E. Baerends, Chem. Phys. Lett. **259**, 599 (1996).
[100] T.-H. Park and P. Nordlander, Chem. Phys. Lett. **472**, 228 (2009).
[101] R. Bardhan, S. Mukherjee, N. A. Mirin, S. D. Levit, P. Nordlander, and N. J. Halas, J. Phys. Chem. C **114**, 7378 (2010).
[102] N. J. Halas, S. Lal, W.-S. Chang, S. Link, and P. Nordlander, Chem. Rev. **111**, 3913 (2011).
[103] E. Prodan, C. Radloff, N. J. Halas, and P. Nordlander, Science **302**, 419 (2003).
[104] P. Nordlander, C. Oubre, E. Prodan, K. Li, and M. I. Stockman, Nano Lett. **4**, 899 (2004).
[105] V. Kulkarni, E. Prodan, and P. Nordlander, Nano Lett. **13**, 5873 (2013).
[106] D.-C. Marinica, J. Aizpurua, and A. G. Borisov, Opt. Express **24**, 23941 (2016).
[107] B. T. Thole, Chem. Phys. **59**, 341 (1981).